Interface Engineering of Metal Oxynitride Lateral Heterojunctions for Photocatalytic and Optoelectronic Applications

Debtanu Maiti, Johnnie Cairns, John N. Kuhn* and Venkat R. Bhethanabotla*

Department of Chemical & Biomedical Engineering, University of South Florida, Tampa, Florida - 33620

ABSTRACT

Significant improvements of the photocatalytic and optoelectronic applications demand materials that exhibit finely tuned band gap, band edge potentials, exciton dynamics, charged states, and crystal facets/edges that facilitate enhanced chemical reactivity. Fundamental insights of the structure-function relationships can dictate the synthesis requirements of these materials. Zinc oxynitride based materials have demonstrated excellent photocatalytic activity and they also present a perfect platform for tailoring the material properties of interest. We hereby investigate lateral heterojunctions of zinc oxynitrides towards applications for photocatalytic and optoelectronic applications by computationally examining their response to composition, lattice strain, and anion vacancy defect variation. Along with tuning the band gap of the materials towards optimal optical performance, we demonstrated the site-specificity of the vacancy defects. Oxygen vacancies and nitrogen vacancies were found to be favored at the bulk and at the interface, respectively. Biaxial and vertical compressive strain increased the band gap, while the tensile strain effected in reduced band gap. The neutral and charged vacancies rendered either increased electronic density of states at the conduction and valence band edges or formation of mid gap states. These insights of electronic state variation via intrinsic material parameters are

Email: jnkuhn@usf.edu (J.N.K.); bhethana@usf.edu (V.R.B.)

fundamental towards synthesis of future materials for enhanced photocatalysis and optoelectronic purposes.

INTRODUCTION

Decline of fossil fuel reserves and the grave consequences of global warming and climate change promoted active research efforts towards sustainable and efficient renewable energy solutions.[1-3] In recent times, solar energy based options have garnered a lot of attention resulting in several significant developments.[4] While photovoltaics, solar water splitting and carbon dioxide reduction are major ways to harvest the abundant solar energy, advances on light emitting diodes (LEDs) and luminescent applications are also necessary for efficient energy utilization. Solar thermochemical approaches have demonstrated superior catalytic activity for water splitting and CO_2 reduction.[5-6] However, they are limited by the high temperatures of operation, while the low temperature photocatalytic and electrocatalytic processes are plagued by other issues like poor rates of conversion, stability, selectivity, and miserable quantum efficiency.[7] Since the first reports of water splitting by Honda and Fujishima in 1972,[8] significant effort has been spent over the last half-century to develop better materials and methods for photocatalytic process.[9]

Material property tuning towards achieving suitable band gap, band edges, morphology, and reduced exciton recombination rates is important for solar photocatalytic processes. While the band gap of a material is the key parameter determining the material's response towards visible light, band edges are primary responsible for the redox reactions. Charge transport and exciton recombination rates are the subsequent controlling parameters that determine the effective utilization of the electrons at the conduction band edge (CBE) and the holes at the

Email: jnkuhn@usf.edu (J.N.K.); bhethana@usf.edu (V.R.B.)

valence band edge (VBE). Even materials having suitable band gaps and band edge potentials can suffer from poor photocatalytic activity due to fast exciton recombination rates. Appropriate band edge potentials, band gap energy along with desired exciton dynamics are thus fundamental requirements for superior photocatalytic activity. Along with these bulk electronic effects, surface morphology effects have a significant role too. While use of extrinsic dopant elements are known to modulate the electronic states of materials, intrinsic parameters like quantum confinement in one or more dimensions, defect concentrations, and lattice strain have also shown promising results.[10-15] Creation of heterojunctions (particularly Type II) have been hailed as one of the most efficient routes for electron hole pair segregation and visible light activity.[16-17] Thus, to achieve effective photocatalysts, it is of prime importance to investigate the effect of these intrinsic parameters – vacancy and strain towards modulating the electronic states of heterojunctions of interest.

Zinc oxide, aluminum nitride, and gallium nitride are well known II-VI and III-V materials mostly stable in hexagonal wurtzite phase, being used for a vast range of applications like gas sensors, LEDs, transistors, and piezoelectric and optoelectronic systems.[14, 18-22] Their solid solutions are well known for catalysis and have even demonstrated highest visible light activity for water splitting.[23-29] Platinum doped zinc oxide-gallium nitride solid solutions have demonstrated CO_2 photoreduction as well.[30] ZnO, AlN and GaN have been used in electronics for a long time and their interfaces are a matter of interesting study for efficient charge transport.[14, 22] These metal oxynitrides, both at the bulk and interface sites, allow for a vast range of composition variation, exhibiting a wide range of electronic density of states. Since, the density of states primarily governs the chemical reactivity and is affected by both strain and vacancy defects, it is of utmost importance to explore the structure-function relationships of

Email: jnkuhn@usf.edu (J.N.K.); bhethana@usf.edu (V.R.B.)

these heterostructures in every detail. Recently research groups have shown promising results on shape control, facet control of materials, along with creation of lateral heterojunctions on substrates.[31-35] In the view of this recent progress on selective facet-controlled material synthesis and on novel heterojunctions fabrication,[31-35] we believe that there lies a huge scope for computationally driven material property prediction for the future synthesis of customized materials of choice.

We hereby present lateral heterojunctions of ZnO:AlN and ZnO:GaN materials for photocatalytic and optoelectronic applications and demonstrate the role of individual material property parameters such as composition, anion vacancy defects, and strain towards modulating the activity of these materials. Along with presenting the role of these intrinsic parameters on the bulk electronic properties of the materials, we reveal the material behavior at the interfaces. The interfaces of ZnO and metal nitrides present a nephelauxetic effect (expansion of electron cloud) due to the increased covalency of the metal-nitrogen bond as opposed to metal-oxygen bonds.[23] Studying these interfaces at their stoichiometric, non-stoichiometric, strained and unstrained forms paves the way for futuristic designs of heterojunctions. Investigation of anion vacancies (in neutral and charged states) at the bulk and at the interfaces provided key site-specific insights on the vacancy formation and the resulting electronic states in these novel heterojunctions. These results are the basis for site-selective catalysis and provide a foundation for rational design of next-generation photocatalytic and optoelectronic materials.

COMPUTATIONAL METHODOLOGY:

The metal oxynitrides have been investigated by spin-polarized density functional theory calculations using Vienna ab-initio Simulation Package (VASP – 5.3.3).[36-38] Plane wave basis sets

Email: jnkuhn@usf.edu (J.N.K.); bhethana@usf.edu (V.R.B.)

have been used throughout. GGA approximation of electron densities was used for calculation of lattice constants, enthalpy of formation, vacancy formation energies and the electronic states. Projector augmented wave (PAW) potentials[37] and Perdew-Burke-Ernzerhof (PBE)[39] exchange correlation were used for most of the calculations. A consistent energy cut off of 600 eV was maintained for all the calculations. We used a 2×2×2 supercell (consisting 32 atoms) for all the basic wurtzite ($P6_3mc$ space group) structures of ZnO, AlN and GaN. The lattice constant was obtained through a series of cell volume relaxation calculations. Gamma centered 8×8×8 kpoint mesh, with symmetry on for k-point reduction, was used for all the 32 atom supercell structures. Electronic density of states was calculated via PBE, HSE06 and GW methods to test the band gap variation as a function of different potentials.

The heterostructures of ZnO, AlN and GaN are made of either 32 atom supercells, 48 atom supercells or 64 atom supercells based on different composition ratios. The k-point mesh was adjusted accordingly to maintain similar grid spacing, while maintaining symmetry (detailed in Table S1). *d* electrons were accounted for the calculations using LMAXMIX flag. The effect of lattice strain was investigated by probing the density of states under strained lattice parameters. The extent of lattice strain in a material has been reported as the percentage deviation from its pure state. Percent vertical strain was defined as $100 \times (c_f - c_i)/c_i$ and percent biaxial strain was defined as $100 \times (a_f - a_i)/a_i$ and $100 \times (b_f - b_i)/b_i$, where '$f$' and '$i$' represents the final and initial values. The neutral and charged vacancy formation was calculated as per the following equation.[40]

$$E_{vac} = E_{Defect\_Mat} - E_{Pure\_Mat} + \sum n_i \mu_i + q E_F$$

Email: jnkuhn@usf.edu (J.N.K.); bhethana@usf.edu (V.R.B.)

While E_{Defect_Mat} is the energy of the non-stoichiometric defect state, E_{Pure_Mat} represents the pure stoichiometric phase energy. E_F is the Fermi level of the material. Thus, E_{vac} is the energy to create a vacancy of n_i atoms of either oxygen or nitrogen (having their respective chemical potentials μ_i). q is the charge associated with the vacancy formation. The charged state of each atom was calculated via Bader analysis.[41-42] All the crystal structure illustrations are made using XCrySDen software.

RESULTS AND DISCUSSIONS

The illustrations of these lateral heterojunctions are revealed in Figures 1 (A-D). The side-projections of hexagonal wurtzite phases of $(ZnO)_X(AlN)_{1-X}$ and $(ZnO)_X(GaN)_{1-X}$ are portrayed in Figures 1A and 1C, respectively, while the top views (Figures 1B and 1D) explicitly reveal the heterojunctions. Different compositions have been studied, ranging from nitride rich phase (X = 0.25) to zinc oxide rich phase (X = 0.75). Based on these composition ratios, the thickness has been varied from one layer (8 atoms) to three layers (24 atoms) of either oxide/nitride phase along the *b* axis of the crystal. These lateral interfaces consist of Ga/Al-O and Zn-N bonds, while periodic continuity has been maintained along the *a* and *c* axes, thus creating periodic potential wells along the *b* axis. The optimized lattice constants (*a, b, c*) of the lateral heterojunctions of ZnO:AlN and ZnO:GaN, as calculated via density functional theory are reported in Table S2. Lattice constants of the pure wurtzite phases of ZnO, AlN and GaN are also documented in Table S2. As observed, the lattice constants increase with increasing ZnO content, synchronous with the trends of lattice constants of pure wurtzite phase of ZnO, AlN and GaN. With increasing ZnO composition in the heterojunctions, the bond lengths between constituent elements show a monotonic increase as well (Table S3, Figures S1 and S2). The

Email: jnkuhn@usf.edu (J.N.K.); bhethana@usf.edu (V.R.B.)

enthalpy of formation reveals increased stability with increased ZnO concentration (Figure 2A). Electronic structure modulation via these lateral heterojunctions is evident from Figure 2B. We

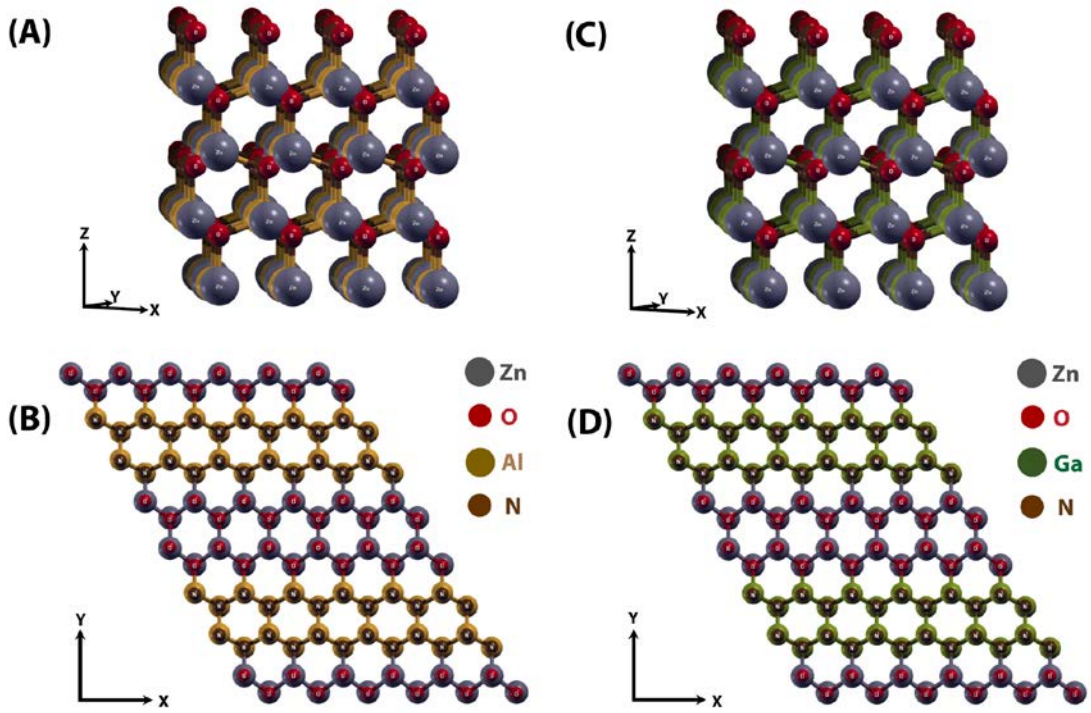

Figure 1: Illustrations of lateral heterojunctions of wurtzite phase $(ZnO)_X(AlN)_{1-X}$ (A-B) and $(ZnO)_X(GaN)_{1-X}$ (C-D)

observe a trend of decreasing band gap with increase in ZnO concentration for both $(ZnO)_X(AlN)_{1-X}$ and $(ZnO)_X(GaN)_{1-X}$. GGA based band gap calculations are known to underestimate the band gap, however they are perfect for observing the trends across a set of materials. Figure S3 reveals that while HSE06 and GW based methods provide more accurate band gap calculations, GGA based methods fare quite well in predicting the trends across different materials. Thus, throughout this article predictions are made based on GGA based calculations. These results are promising for material property tuning simply by composition variation. This resulting reduction in band gap from that of pure phase ZnO, AlN and GaN is often attributed to the Zn-3d and O-2p and N-2p repulsion[18, 22], and allows for these heterojunctions to perform in visible light applications.

Email: jnkuhn@usf.edu (J.N.K.); bhethana@usf.edu (V.R.B.)

These heterojunctions are intrinsically strained as is evident from the lattice constant values. When these are grown on substrates with different lattice constants, these structures are even more strained. There are evidences of substrate induced strain and tuning material properties for catalytic and optoelectronic purposes.[43-47] Hence, an investigation on the effects of strain towards tuning the electronic states is of prime importance. We observe an increased band gap with biaxial compression and the reduction of band gap with tensile relaxation for the $(ZnO)_X(AlN)_{1-X}$ systems (Figure 2C). For $(ZnO)_X(GaN)_{1-X}$ heterostructures (Figure 2D), both biaxial and vertical compression effect in increased band gap, while causing reduction of the band gap under tensile relaxation. Figure S4 portrays the strain tuning of the pure materials like ZnO, AlN and GaN. While the changing bulk density due to strained lattice parameters has a role in tuning the band gap, the inherent material responses towards different strains cannot be ignored. Figure S4 (B) portrays the tolerance of AlN towards vertical strain while being easily tuned under biaxial strain. ZnO on the contrary is more affected by the vertical strain. The VBE of these materials are known to comprise of the antibonding states of Zn-3d or O-2p or N-2p, while the CBE is mostly dominated by the antibonding states of s-p orbitals of the metals. With lattice compression, the bonding orbitals are stabilized and the antibonding orbitals are destabilized.[11, 48-49] CBE being more perturbed by the strain effects,[11] there is net increase of band gap with compression and vice versa with tension. Moreover, it is also revealed that the biaxial strain is more effective than the vertical strain in tuning band gap of these lateral heterojunctions. This may be due to the fact that the VBE is comprised mostly of the N-2p orbital, followed by Zn-3d and O-2p[18,22], and therefore the p-d repulsion between Zn-3d and N-2p, which is accentuated by strain normal to the interface (i.e. biaxial), will have the greatest effect on the band gap. Figures 2(E-H) depict the shift of the density of states of the Zn-3d

Email: jnkuhn@usf.edu (J.N.K.); bhethana@usf.edu (V.R.B.)

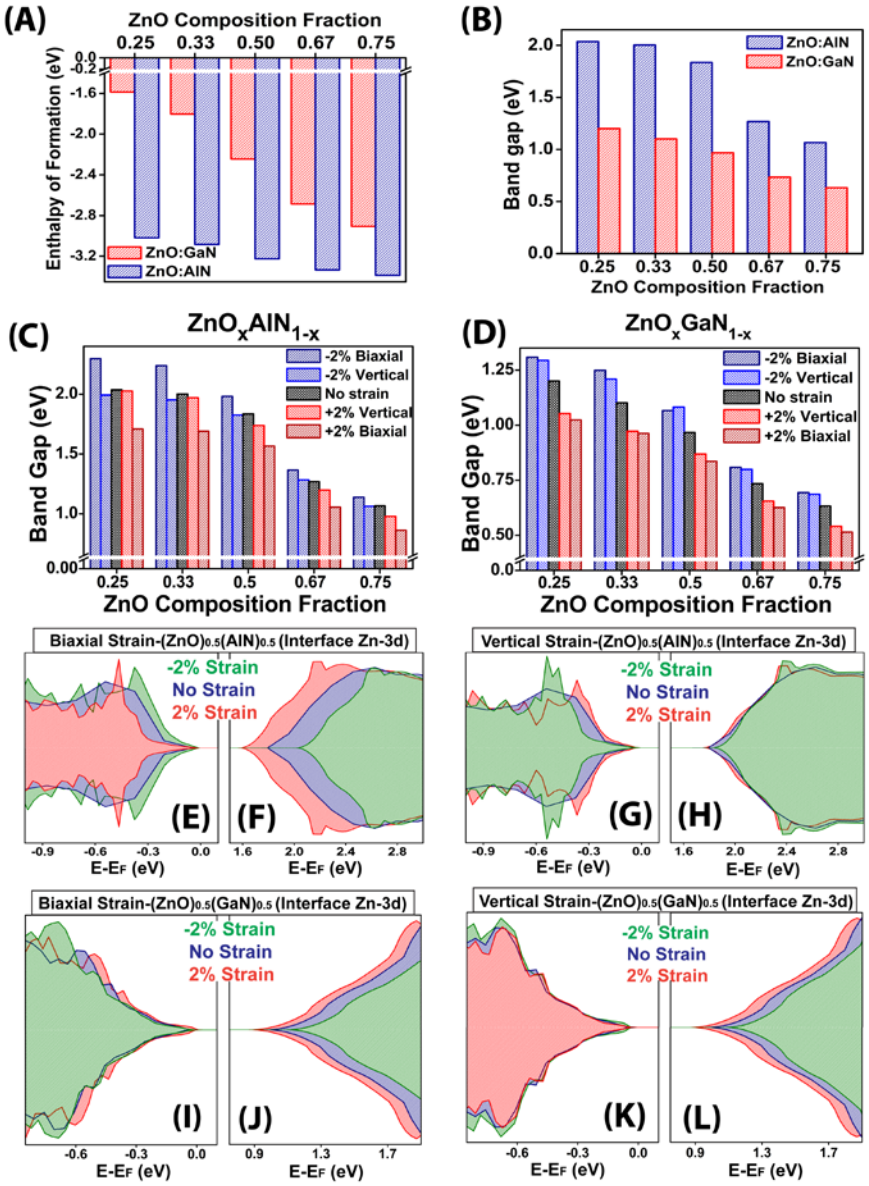

Figure 2: Enthalpy of formation (A) and band gap variation (B) for $(ZnO)_X(AlN)_{1-X}$ and $(ZnO)_X(GaN)_{1-X}$ with varying composition. Band gap tuning of $(ZnO)_X(AlN)_{1-X}$ (C) and $(ZnO)_X(GaN)_{1-X}$ (D) via biaxial and vertical tensile and compressive strain. Modulation of electronic density of states of Zn-3d orbital of $(ZnO)_{0.5}(AlN)_{0.5}$ along the VBE and CBE under biaxial strain (E-F) and under vertical strain (G-H). Modulation of electronic density of states of Zn-3d orbital of $(ZnO)_{0.5}(GaN)_{0.5}$ along the VBE and CBE under biaxial strain (I-J) and under vertical strain (K-L).

orbital across the VBE and CBE of $(ZnO)_{0.5}(AlN)_{0.5}$. The y-axis of the DOS plots represents the density of states (states/eV) with the positive and negative axes corresponding to spin-up and

Email: jnkuhn@usf.edu (J.N.K.); bhethana@usf.edu (V.R.B.)

spin-down states. The valence band edge (VBE) has been aligned to $E-E_F = 0$. Thus the band gap variation due to different strain is revealed by the conduction band edge (CBE) position. As per Figure 2F, we see the CBE of $(ZnO)_{0.5}(AlN)_{0.5}$ being shifted far right under biaxial compression (green shaded area) and shifted to the left under biaxial tensile relaxation (red shaded area). This portrays the effect of biaxial strain on each of the interfacial atoms that effects the band gap modulation. Figure 2(G-H) depicts the effects of vertical strain on the interfacial Zn-3d orbitals. Though the projected density of states is shifted right under compression and vice-versa, the effects are less pronounced than that under biaxial strain. Similar patterns have been plotted for $(ZnO)_{0.5}(GaN)_{0.5}$ (Figures 2(I-L)), and the effects of vertical and biaxial strain are similar. Under both biaxial compression (Figure 2J) and vertical compression (Figure 2L), we demonstrate right shift of the CBE of interfacial Zn-3d orbitals (green shaded area). Overall biaxial strain is found to have a much more pronounced effect than vertical strain on $(ZnO)_{0.5}(AlN)_{0.5}$, while for $(ZnO)_{0.5}(GaN)_{0.5}$ the effects are quite close. This can be attributed to lattice mismatch of the heterostructures and the intrinsic band gap tunability traits of AlN under biaxial strain (Figures S4-B). The lattice mismatch of ZnO and AlN is much more than that of ZnO and GaN. This is also reflected in the lattice constant values (Table S2) of these heterojunctions. Thus, the effect of biaxial strain (normal to the interface) is more prominent for $(ZnO)_X(AlN)_{1-X}$ than $(ZnO)_X(GaN)_{1-X}$. Understanding these effects of strain on the band gap and band edges is essential for tailoring these heterojunctions towards specific applications. Additionally, knowledge of the behavior of atomic orbitals at the band edges, particularly at the VBE, is critical for predicting light absorption properties.

Since it is the interface that exhibits under/over coordinated sites and charge accumulation/depletion, we probed the atom projected density of states of different constituent

Email: jnkuhn@usf.edu (J.N.K.); bhethana@usf.edu (V.R.B.)

elements at their bulk and interface locations. A detailed schematic of the bulk and interface atoms in these lateral heterojunctions is provided in Figure S5. Figures 3(A-D) show the electronic density of states of Zn, O, Al and N orbitals across the VBE and CBE of $(ZnO)_{0.25}(AlN)_{0.75}$. Every atom in this wurtzite phase is tetrahedrally coordinated to four other atoms. For a zinc atom in its bulk location, all the four nearest neighbor atoms are oxygen, while an interface zinc atom interacts with one nitrogen atom and three oxygen atoms. Nitrogen is a less electronegative element than oxygen, and thus the metal-nitrogen bond is more covalent in nature causing a decrease in the oxidation state of the interface zinc atom. This difference in the electronic charge accumulation for a bulk and an interface atom of zinc is shown in Figure 3A where we plot only the most dominant Zn orbital along the VBE (Zn-3d). Such charge accumulation at interface atoms allows enrichment of these heterojunctions with catalytic active sites without the need for less-abundant external dopants. The most dominant orbital along the CBE for zinc is the 4s orbital. It is also depicted that the bulk zinc atoms exhibit higher electronic density of states across the CBE than the interface atoms. Table S4 documents the oxidation states of all the elements across bulk and interfaces of these $(ZnO)_X(AlN)_{1-X}$ and $(ZnO)_X(GaN)_{1-X}$ heterojunctions. For aluminum, the most dominant orbital across the VBE and CBE is the 3p orbital. The oxidation states (Table S4) are similar across bulk and interface and that is reflected in the VBE (Figure 3C), however the CBE shows proliferation of empty 3p-electronic density of states at the interface compared to that of the bulk elements. The interface effects on the O-2p electronic density of states are shown in Figure 3B while the same for N-2p is depicted in Figure 3D. This variation in the electronic density of states of all the elements are witness to enhanced catalytic reactivity at the interfaces. The difference of charge states are already reported in Table S4. A similar trend (Figures 3E-3H) is observed for $(ZnO)_{0.25}(GaN)_{0.75}$

Email: jnkuhn@usf.edu (J.N.K.); bhethana@usf.edu (V.R.B.)

as well. These electronic density of states at the bulk/interface maintain their traits even under strained conditions as shown in Figure S6.

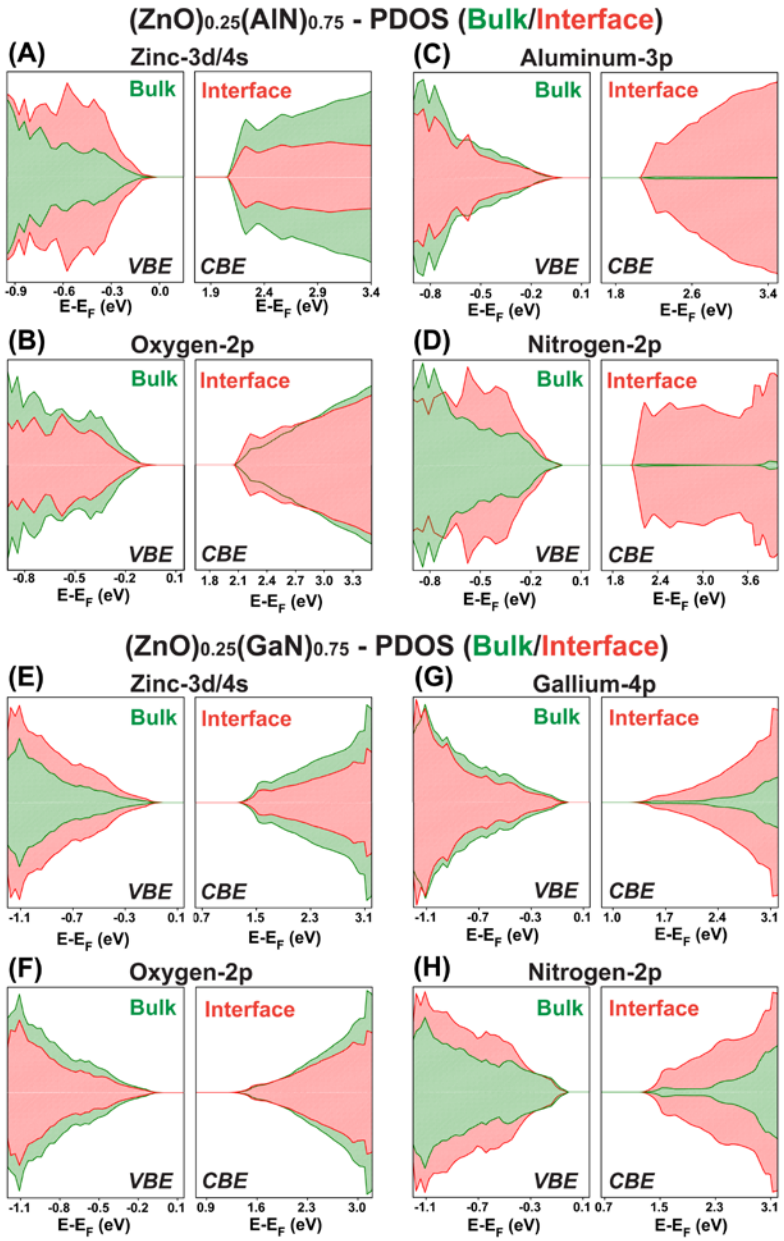

Figure 3: Variation of the electronic density of states of the most prominent orbitals across VBE and CBE for zinc (A), oxygen (B), aluminum (C) and nitrogen (D) at the bulk and interface sites for $(ZnO)_{0.25}(AlN)_{0.75}$. Variation of the electronic density of states of the most prominent orbitals across VBE and CBE for zinc (E), oxygen (F), gallium (G) and nitrogen (H) at the bulk and interface sites for $(ZnO)_{0.25}(GaN)_{0.75}$.

Email: jnkuhn@usf.edu (J.N.K.); bhethana@usf.edu (V.R.B.)

The site-specific variation of the charge states and electronic density of states is directly linked to the vacancy formation characteristics of these materials. Catalysis over defect sites are well known and it is of prime importance to explore the vacancy formation phenomenon over these heterojunctions. Vacancy defect states act as charge traps and have direct influence on the charge transport properties. We report the oxygen and nitrogen vacancy formation energies in $(ZnO)_X(AlN)_{1-X}$ and $(ZnO)_X(GaN)_{1-X}$ (Figures 4A-D). Anion vacancies are known to exist in either neutral or charged states. Oxygen vacancies are reported to be mostly stable in +2 state in ZnO, while in neutral state under highly n-type conditions.[40] The DFT based methodology has known issues with calculating band gap for charged defects due the finite size supercell effects and due to the intrinsic DFT failure with electronic band gap prediction.[50] Since large supercell DFT calculations of charged systems are computationally expensive, we restricted ourselves only to selective sets of charged vacancy calculations. For $(ZnO)_X(AlN)_{1-X,}$ the oxygen vacancy formation energy at its neutral state was found to be favorable in the bulk as opposed to the interface sites. This is attributed to the difference in the oxidation states of oxygen at the bulk and interface (Table S4). An oxygen atom at the interface is more reduced (stronger bonds) and demands a higher energy input to create a vacancy. The opposite trend is observed with nitrogen vacancy, where the bulk nitrogen atom exhibits a stronger bond, thereby being more reluctant towards vacancy formation. This trend of site-selective vacancy formation was observed in $(ZnO)_X(GaN)_{1-X}$ as well irrespective of the material composition. (Figures. 4C-D).

Email: jnkuhn@usf.edu (J.N.K.); bhethana@usf.edu (V.R.B.)

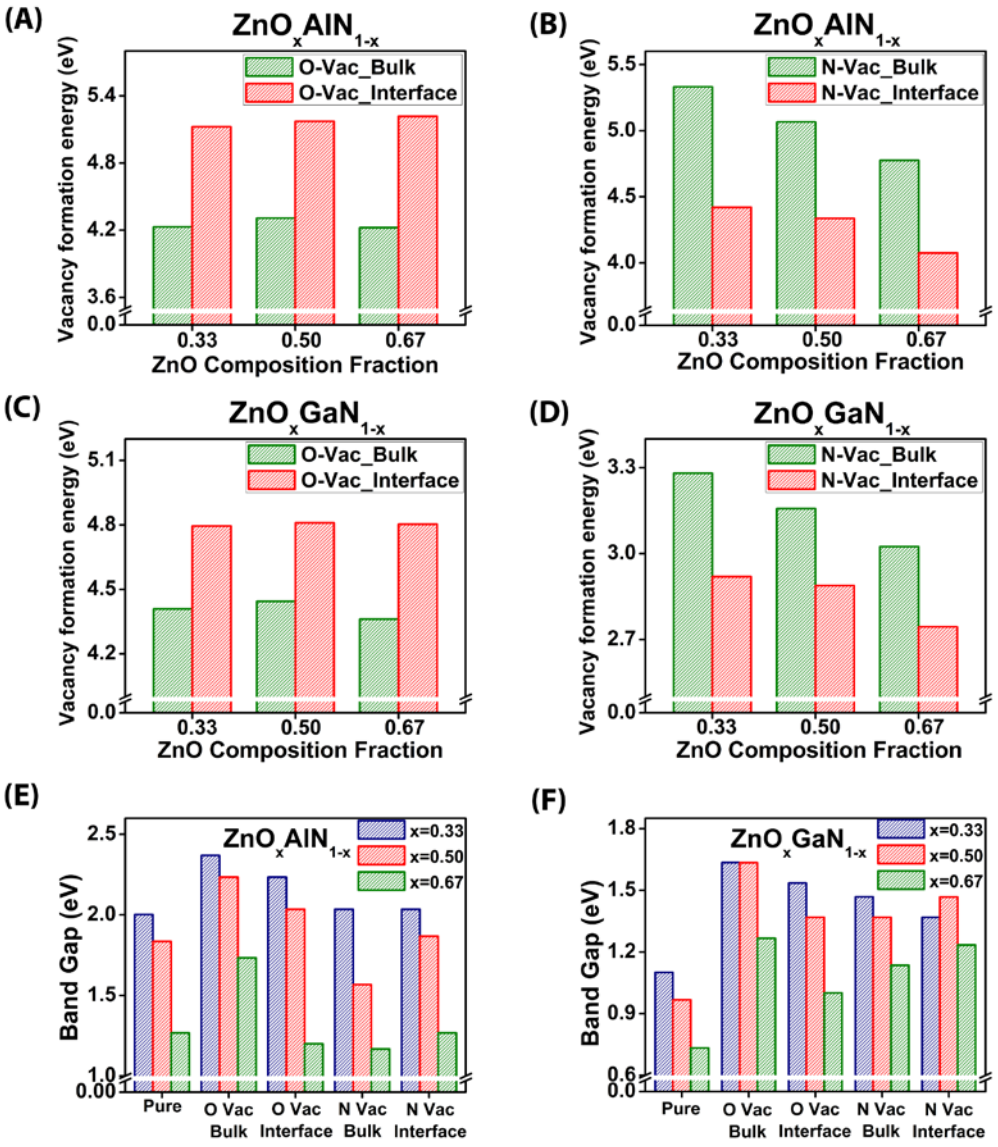

Figure 4: Oxygen vacancy (neutral) formation energy in $(ZnO)_X(AlN)_{1-X}$ (A) and $(ZnO)_X(GaN)_{1-X}$ (C). Nitrogen vacancy (neutral) formation energy in $(ZnO)_X(AlN)_{1-X}$ (B) and $(ZnO)_X(GaN)_{1-X}$ (D). Band gap variations in stoichiometric and non-stoichiometric $(ZnO)_X(AlN)_{1-X}$ (E) and $(ZnO)_X(GaN)_{1-X}$ (F).

Site dependent vacancy formation energy is the key towards understanding preferred vacancy formation under real experimental conditions. The role of these vacancies towards tuning the electronic band gap is depicted in Figures 4 (E-F). We do observe a substantial change in band gap due to the presence of vacancies, and for all the vacant systems, the trend is

Email: jnkuhn@usf.edu (J.N.K.); bhethana@usf.edu (V.R.B.)

consistent across the material composition. The formation energy of (+2) charged oxygen vacancy in $(ZnO)_X(AlN)_{1-X}$ is reported in Figure 5A. The charged vacancy formation was found to be more favorable than the neutral ones (Figure 4A). We also find that the preferred site for vacancy formation is still in the bulk, and not at the interface (lower vacancy formation energies at the bulk, Figure 5A). The effect of oxygen vacancies (+2) at the bulk and interface sites on the electronic states of $(ZnO)_{0.5}(AlN)_{0.5}$ is shown in Figure 5B. Interestingly we observe that there are mid-gap states being generated due to the vacancies, which will effectively increase the ability of these vacant materials to produce excitons or can also act as trap states. Generation of electronic mid-gap states is also found in oxygen vacant $(ZnO)_{0.25}(AlN)_{0.75}$ and $(ZnO)_{0.75}(AlN)_{0.25}$ under (+2) charged states (Figures S7(A-B)).

In order to have a better understanding of the oxygen vacant sites of $(ZnO)_{0.5}(AlN)_{0.5}$, the electronic density of states of the nearest neighboring zinc atoms are plotted (Figures 5C-H). Every oxygen atom in a stoichiometric pure $(ZnO)_{0.5}(AlN)_{0.5}$ is tetrahedrally surrounded by four atoms (detailed in Figure S5). A bulk oxygen atom has four zinc atoms as its neighbors while the interface one has three atoms of zinc and one aluminum atom. Similar coordination pattern exists for a zinc atom as well, where an interface zinc atom has only three oxygen neighboring atoms and a bulk zinc atom has all four oxygen atoms as neighbors. In this scenario, it is possible to locate a bulk zinc atom in $(ZnO)_{0.5}(AlN)_{0.5}$ which has an interface oxygen atom as well as a bulk oxygen atom as its neighbors. Similarly, it is also possible to locate an interface zinc atom with both an interface oxygen atom as well as a bulk oxygen atom as its neighbors. This presents a perfect platform for studying the effect of bulk and interface oxygen vacancies in both neutral and charged states. The evolution of density of states of the Zn 4s, 4p and 3d orbitals from their

Email: jnkuhn@usf.edu (J.N.K.); bhethana@usf.edu (V.R.B.)

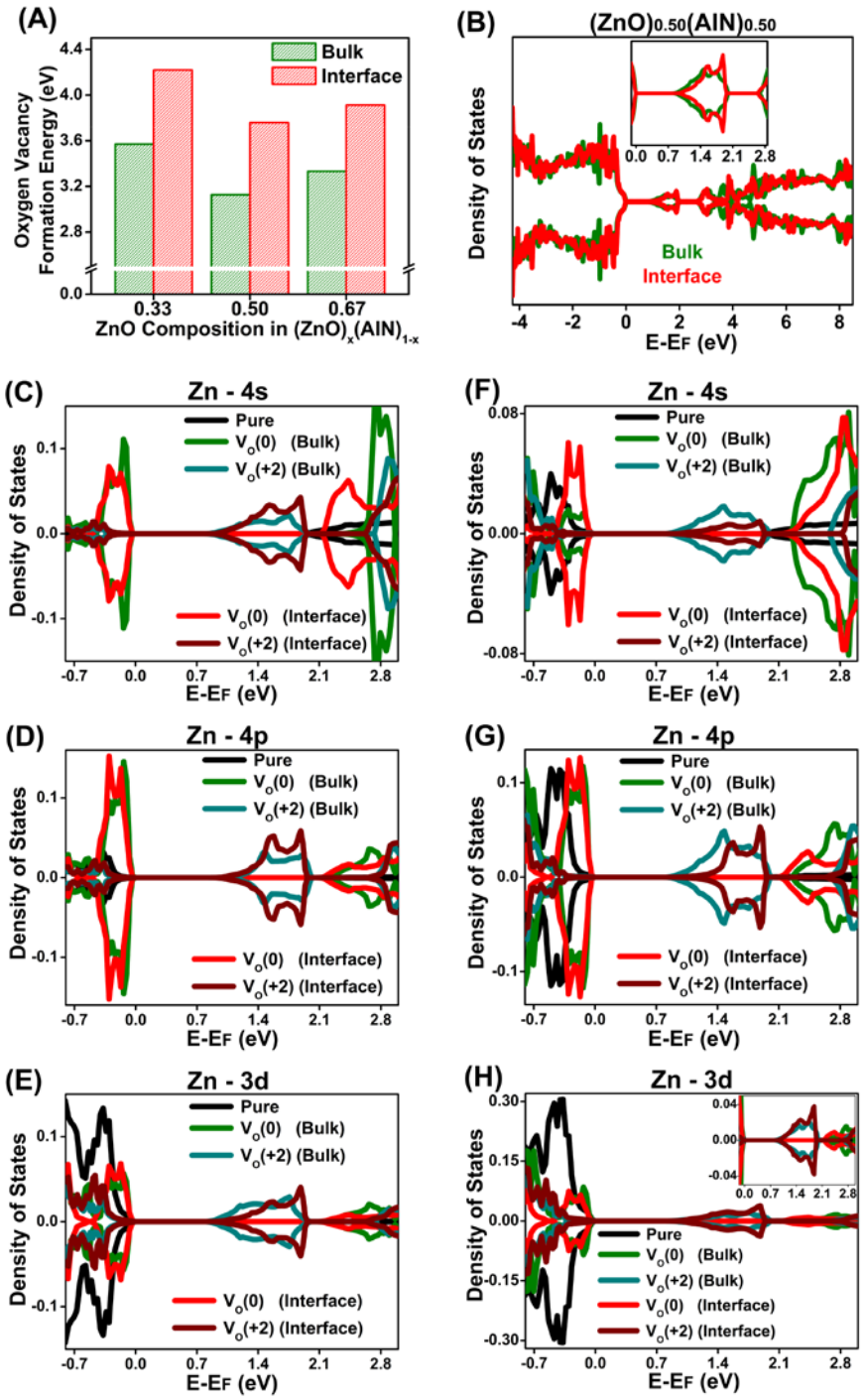

Figure 5: (A) Charged oxygen vacancy (+2) formation energy in $(ZnO)_X(AlN)_{1-X}$. (B) The density of states of zinc atoms neighboring a bulk and an interface oxygen vacancy. (C-E) DOS of a bulk Zn (4s, 4p, 3d) atom neighboring bulk and interface oxygen vacancies in neutral and charged states. (F-H) DOS of an interface Zn (4s, 4p, 3d) atom neighboring bulk and interface oxygen vacancies in neutral and charged states.

Email: jnkuhn@usf.edu (J.N.K.); bhethana@usf.edu (V.R.B.)

pure state to oxygen vacant form is thus revealed in Figures 5C-E respectively. Proliferation of 4s and 4p orbital density of states across VBE and CBE on the formation of a neutral oxygen vacancy is noted, along with increase of band gap due to the increased repulsion of the electron cloud. This is justified by the decrease of zinc oxidation states due to the formation of neutral vacancies both across the bulk and interfaces respectively (Table S5). There also exists a minor site-specific vacancy effect on the extent of increase of VBE states, which affects light absorption properties. The extent of electron accumulation on a bulk zinc atom due to the formation of a nearby bulk oxygen vacancy is more than that compared to a nearby interface oxygen vacancy (Table S5). This leads to more enhanced of VBE states of Zn-4s and Zn-4p under bulk oxygen vacant condition as opposed to interface oxygen vacancy states (Figures 5C-D).

On the contrary, a reverse effect is observed when a charged oxygen vacancy is formed. In that scenario, the electron accumulation on a bulk zinc atom is more when an interface oxygen vacancy is present and vice-versa. This allows a bulk zinc 4s and 4p orbitals to contribute towards increased mid-gap state formation when an interface oxygen vacancy is formed and vice versa (Figures 5C-D and 5F-G). Figures 5 (F-H) depicts the evolution of 4s, 4p, and 3d orbital density of states of an interface zinc atom under the influence of both bulk and interface oxygen vacancies at neutral and charged states. This reverse trend of electron accumulation effects on zinc atom under bulk/interface oxygen vacancies is closely related to crystal relaxation pattern during vacancy formation. As observed in ZnO systems, an oxygen vacancy results in four dangling zinc-oxygen bonds in a *a1* symmetry. In the case of neutral vacancies, this state has two electrons, while in the case of charged vacancies, this state has none. This drives the local crystal

Email: jnkuhn@usf.edu (J.N.K.); bhethana@usf.edu (V.R.B.)

relaxation in opposite directions. We also observed a similar relaxation pattern in our $(ZnO)_{0.5}(AlN)_{0.5}$ materials, whereby the four dangling zinc atoms try to collapse towards the vacant site (move inwards) for a neutral vacancy, while for a charged vacancy, they relax outwards (Table S6). The nearby Zn-O bond length is a measure of this change – increased bond length for neutral vacancies and decreased bond lengths for charged vacancy (Table S6). In a similar fashion, $(ZnO)_{0.5}(GaN)_{0.5}$ exhibits these trends under neutral and charged vacancy as well (density of states shown in Figure S8). These effects of vacancy formation both under neutral and charged states for these lateral heterojunctions are of acute interest for site specific catalytic reactions.

CONCLUSIONS

These results are a manifestation of the vast capabilities of these materials to be tuned as per custom requirements. Intrinsic material parameters like composition, strain and vacancies can translate to substantial changes in the electronic properties of these heterojunctions. The site-specific anion vacancies over these heterojunctions offer avenues for tuning vacancy concentration and location at different reaction/synthesis conditions. It has already been reported that even CO_2 adsorption energy, a key descriptor of CO_2 conversion reactions, increases with oxygen vacancies.[16, 51] With precise control of site specific defect creation, strain and composition tuning, we anticipate these materials are potential candidates for any photocatalytic water/carbon dioxide splitting purposes as well as for optoelectronic devices. With the advance of experimental protocols, we strongly believe these next generation materials can be fabricated for their application in energy efficient solutions.

Email: jnkuhn@usf.edu (J.N.K.); bhethana@usf.edu (V.R.B.)

SUPPORTING INFORMATION:

Figures for bond length variation, pure phase (ZnO, AlN and GaN) band gap calculation, strain effects on band gap of pure phase materials, detailed schematic of the lateral heterojunction, strain induced Zn-3d orbital PDOS variation, DOS for oxynitrides under charged oxygen vacant conditions.

Tables for k-point information, DFT optimized lattice constants, bond lengths, oxidation states of each atoms of stoichiometric compounds, variation of oxidation states of zinc atom neighboring oxygen vacancies, Zn-O bond lengths around oxygen vacant sites.

CONFLICTS OF INTEREST:

The authors declare no competing financial interests related to this work.

ACKNOWLEDGEMENTS:

The authors would like to appreciate USF Research Computing for the high performance computing resources. Financial support from NSF grants IIP 1743623 and CHE 1531590 are greatly appreciated. DM acknowledges the dissertation completion fellowship from the Office of Graduate Studies, USF for financial support.

REFERENCES:

(1) Centi, G.; Quadrelli, E. A.; Perathoner, S. Catalysis for CO_2 Conversion: A Key Technology for Rapid Introduction of Renewable Energy in the Value Chain of Chemical Industries. *Energy Environ. Sci.* **2013**, *6*, 1711-1731.

(2) Olivier, J. G. J.; Janssens-Maenhout, G.; Muntean, M.; Peters, J. A. H. W. *Trends in Global CO_2 Emissions*. **2016**, 1-86.

Email: jnkuhn@usf.edu (J.N.K.); bhethana@usf.edu (V.R.B.)

(3) Chen, S.; Takata, T.; Domen, K. Particulate Photocatalysts for Overall Water Splitting. *Nat. Rev. Mater.* **2017**, *2*, 17050.

(4) Steinfeld, A.; Palumbo, R. Solar Thermochemical Process Technology. *Encyclopedia of Physical Science & Technology*, Meyers, R. A., Ed. Academic Press. **2001**, Vol. 15, 237-256.

(5) Chueh, W. C.; Falter, C.; Abbott, M.; Scipio, D.; Furler, P.; Haile, S. M.; Steinfeld, A. High-Flux Solar-Driven Thermochemical Dissociation of CO_2 and H_2O Using Nonstoichiometric Ceria. *Science* **2010**, *330*, 1797-1801.

(6) Maiti, D.; Hare, B. J.; Daza, Y. A.; Ramos, A. E.; Kuhn, J. N.; Bhethanabotla, V. R. Earth Abundant Perovskite Oxides for Low Temperature CO_2 Conversion. *Energy Environ. Sci.* **2018**, *11*, 648-659.

(7) Yuan, L.; Xu, Y.-J. Photocatalytic Conversion of CO_2 into Value-Added and Renewable Fuels. *Appl. Surf. Sci.* **2015**, *342*, 154-167.

(8) Fujishima, A.; Honda, K. Electrochemical Photolysis of Water at a Semiconductor Electrode. *Nature* **1972**, *238*, 37.

(9) Li, K.; An, X.; Park, K. H.; Khraisheh, M.; Tang, J. A Critical Review of CO_2 Photoconversion: Catalysts and Reactors. *Catal. Today* **2014**, *224*, 3-12.

(10) Chen, Y.; Xi, J.; Dumcenco, D. O.; Liu, Z.; Suenaga, K.; Wang, D.; Shuai, Z.; Huang, Y. S.; Xie, L. Tunable Band Gap Photoluminescence from Atomically Thin Transition-Metal Dichalcogenide Alloys. *ACS Nano* **2013**, *7*, 4610-4616.

(11) Lu, Y. B.; Dai, Y.; Wei, W.; Zhu, Y.; Huang, B. Strain-Engineered Modulation on the Electronic Properties of Phosphorous-Doped Zno. *ChemPhysChem* **2013**, *14*, 3916-3924.

Email: jnkuhn@usf.edu (J.N.K.); bhethana@usf.edu (V.R.B.)

(12) Terrones, H.; Lopez-Urias, F.; Terrones, M. Novel Hetero-Layered Materials with Tunable Direct Band Gaps by Sandwiching Different Metal Disulfides and Diselenides. *Sci. Rep.* **2013**, *3*, 1549.

(13) Wang, J.; Wang, Z.; Huang, B.; Ma, Y.; Liu, Y.; Qin, X.; Zhang, X.; Dai, Y. Oxygen Vacancy Induced Band-Gap Narrowing and Enhanced Visible Light Photocatalytic Activity of ZnO. *ACS Appl. Mater. Interfaces* **2012**, *4*, 4024-4030.

(14) Yang, L.; Liu, W.; Xu, H.; Ma, J.; Zhang, C.; Liu, C.; Wang, Z.; Liu, Y. Enhanced near-UV Electroluminescence from p-GaN/i-Al_2O_3/n-ZnO Heterojunction Leds by Optimizing the Insulator Thickness and Introducing Surface Plasmons of Ag Nanowires. *J. Mater. Chem. C* **2017**, *5*, 3288-3295.

(15) Bai, S.; Wang, L.; Li, Z.; Xiong, Y. Facet-Engineered Surface and Interface Design of Photocatalytic Materials. *Adv. Sci.* **2016**, *4*, 1600216.

(16) Reza Gholipour, M.; Dinh, C.-T.; Beland, F.; Do, T.-O. Nanocomposite Heterojunctions as Sunlight-Driven Photocatalysts for Hydrogen Production from Water Splitting. *Nanoscale* **2015**, *7*, 8187-8208.

(17) Low, J.; Yu, J.; Jaroniec, M.; Wageh, S.; Al-Ghamdi Ahmed, A. Heterojunction Photocatalysts. *Adv. Mater.* **2017**, *29*, 1601694.

(18) Chen, C.; Shang, Z.; Gong, J.; Zhang, F.; Zhou, H.; Tang, B.; Xu, Y.; Zhang, C.; Yang, Y.; Mu, X. Electric Field Stiffening Effect in c-Oriented Aluminum Nitride Piezoelectric Thin Films. *ACS Appl. Mater. Interfaces* **2018**, *10*, 1819-1827.

(19) Kim, K. H.; Lee, T. H.; Kim, T. G. AlN/ITO-Based Hybrid Electrodes with Conducting Filaments: Their Application to Ultraviolet Light-Emitting Diodes. *ACS Appl. Mater. Interfaces* **2017**, *9*, 24357-24364.

Email: jnkuhn@usf.edu (J.N.K.); bhethana@usf.edu (V.R.B.)

(20) Golgir, H. R.; Li, D. W.; Keramatnejad, K.; Zou, Q. M.; Xiao, J.; Wang, F.; Jiang, L.; Silvain, J.-F.; Lu, Y. F. Fast Growth of Gan Epilayers Via Laser-Assisted Metal-Organic Chemical Vapor Deposition for Ultraviolet Photodetector Applications. *ACS Appl. Mater. Interfaces* **2017**, *9*, 21539-21547.

(21) Park, S.; An, S.; Ko, H.; Jin, C.; Lee, C. Synthesis of Nanograined ZnO Nanowires and Their Enhanced Gas Sensing Properties. *ACS Appl. Mater. Interfaces* **2012**, *4*, 3650-3656.

(22) Lupan, O.; Pauporté, T.; Viana, B. Low-Voltage UV-Electroluminescence from ZnO-Nanowire Array/p-Gan Light-Emitting Diodes. *Adv. Mater.* **2010**, *22*, 3298-3302.

(23) Fuertes, A. Metal Oxynitrides as Emerging Materials with Photocatalytic and Electronic Properties. *Mater. Horiz.* **2015**, *2*, 453-461.

(24) Maeda, K.; Domen, K. Solid Solution of GaN and ZnO as a Stable Photocatalyst for Overall Water Splitting under Visible Light. *Chem. Mater.* **2010**, *22*, 612-623.

(25) Dionigi, F.; Vesborg, P. C. K.; Pedersen, T.; Hansen, O.; Dahl, S.; Xiong, A.; Maeda, K.; Domen, K.; Chorkendorff, I. Suppression of the Water Splitting Back Reaction on GaN:ZnO Photocatalysts Loaded with Core/Shell Cocatalysts, Investigated Using a M-Reactor. *J. Catal.* **2012**, *292*, 26-31.

(26) Maeda, K.; Teramura, K.; Takata, T.; Hara, M.; Saito, N.; Toda, K.; Inoue, Y.; Kobayashi, H.; Domen, K. Overall Water Splitting on $(Ga_{1-X}Zn_x)(N_{1-X}O_x)$ Solid Solution Photocatalyst: Relationship between Physical Properties and Photocatalytic Activity. *J. Phys. Chem. B* **2005**, *109*, 20504-20510.

(27) Maeda, K.; Domen, K. Photocatalytic Water Splitting: Recent Progress and Future Challenges. *J. Phys. Chem. Lett.* **2010**, *1*, 2655-2661.

Email: jnkuhn@usf.edu (J.N.K.); bhethana@usf.edu (V.R.B.)

(28) Maeda, K.; Takata, T.; Hara, M.; Saito, N.; Inoue, Y.; Kobayashi, H.; Domen, K. GaN:ZnO Solid Solution as a Photocatalyst for Visible-Light-Driven Overall Water Splitting. *J. Am. Chem. Soc.* **2005**, *127*, 8286-8287.

(29) Ohno, T.; Bai, L.; Hisatomi, T.; Maeda, K.; Domen, K. Photocatalytic Water Splitting Using Modified GaN:ZnO Solid Solution under Visible Light: Long-Time Operation and Regeneration of Activity. *J. Am. Chem. Soc.* **2012**, *134*, 8254-8259.

(30) Zhou, P.; Wang, X.; Yan, S.; Zou, Z. Solid Solution Photocatalyst with Spontaneous Polarization Exhibiting Low Recombination toward Efficient CO_2 Photoreduction. *ChemSusChem* **2016**, *9*, 2064-2068.

(31) Polo-Garzon, F.; Yang, S. Z.; Fung, V.; Foo Guo, S.; Bickel Elizabeth, E.; Chisholm Matthew, F.; Jiang, D. e.; Wu, Z. Controlling Reaction Selectivity through the Surface Termination of Perovskite Catalysts. *Angew. Chem. Int. Ed.* **2017**, *129*, 9952-9956.

(32) Sahoo, P. K.; Memaran, S.; Xin, Y.; Balicas, L.; Gutiérrez, H. R. One-Pot Growth of Two-Dimensional Lateral Heterostructures Via Sequential Edge-Epitaxy. *Nature* **2018**, *553*, 63-67.

(33) Gong, Y.; Lin, J.; Wang, X.; Shi, G.; Lei, S.; Lin, Z.; Zou, X.; Ye, G.; Vajtai, R.; Yakobson, B. I.; et al. Vertical and in-Plane Heterostructures from WS_2/MoS_2 Monolayers. *Nat. Mater.* **2014**, *13*, 1135-1142.

(34) Najmaei, S.; Zou, X.; Er, D.; Li, J.; Jin, Z.; Gao, W.; Zhang, Qi.; Park, S.; Ge, L.; Lei, G.; et al. Tailoring the Physical Properties of Molybdenum Disulfide Monolayers by Control of Interfacial Chemistry. *Nano Lett.* **2014**, *14*, 1354-1361.

(35) Huang, M.; Weng, S.; Wang, B.; Hu, J.; Fu, X.; Liu, P. Various Facet Tunable ZnO Crystals by a Scalable Solvothermal Synthesis and Their Facet-Dependent Photocatalytic Activities. *J. Phys. Chem. C* **2014**, *118*, 25434-25440.

Email: jnkuhn@usf.edu (J.N.K.); bhethana@usf.edu (V.R.B.)

(36) Hohenberg, P.; Kohn, W. Inhomogeneous Electron Gas. *Phys. Rev.* **1964**, *136*, B864-B871.

(37) Kresse, G.; Joubert, D. From Ultrasoft Pseudopotentials to the Projector Augmented-Wave Method. *Phys. Rev. B* **1999**, *59*, 1758-1775.

(38) Kresse, G.; Furthmüller, J. Efficient Iterative Schemes for *Ab Initio* Total-Energy Calculations Using a Plane-Wave Basis Set. *Phys. Rev. B* **1996**, *54*, 11169-11186.

(39) Perdew, J. P.; Burke, K.; Ernzerhof, M. Generalized Gradient Approximation Made Simple. *Phys. Rev. Lett.* **1996**, *77*, 3865-3868.

(40) Janotti, A.; Van de Walle, C. G. Oxygen Vacancies in ZnO. *Appl. Phys. Lett.* **2005**, *87*, 122102.

(41) Tang, W.; Sanville, E.; Henkelman, G. A Grid-Based Bader Analysis Algorithm without Lattice Bias. *J. Phys.: Condens. Matter* **2009**, *21*, 084204.

(42) Henkelman, G.; Arnaldsson, A.; Jónsson, H. A Fast and Robust Algorithm for Bader Decomposition of Charge Density. *Comput. Mater. Sci.* **2006**, *36*, 354-360.

(43) Shinde, S. R.; Ramesh, R.; Lofland, S. E.; Bhagat, S. M.; Ogale, S. B.; Sharma, R. P.; Venkatesan, T. Effect of Lattice Mismatch Strains on the Structural and Magnetic Properties of Barium Ferrite Films. *Appl. Phys. Lett.* **1998**, *72*, 3443-3445.

(44) McTague, J. P.; Novaco, A. D. Substrate-Induced Strain and Orientational Ordering in Adsorbed Monolayers. *Phys. Rev. B* **1979**, *19*, 5299-5306.

(45) Smith, A. M.; Mohs, A. M.; Nie, S. Tuning the Optical and Electronic Properties of Colloidal Nanocrystals by Lattice Strain. *Nat. Nanotechnol.* **2009**, *4*, 56-63.

Email: jnkuhn@usf.edu (J.N.K.); bhethana@usf.edu (V.R.B.)

(46) Sun, W.; Zhou, Z.; Zaman, W. Q.; Cao, L.-m.; Yang, J. Rational Manipulation of IrO_2 Lattice Strain on α-MnO_2 Nanorods as a Highly Efficient Water-Splitting Catalyst. *ACS Appl. Mater. Interfaces* **2017**, *9*, 41855-41862.

(47) Hutchings, G. S.; Jhang, J.-H.; Zhou, C.; Hynek, D.; Schwarz, U. D.; Altman, E. I. Epitaxial Ni_XPd_{1-X} (111) Alloy Substrates with Continuously Tunable Lattice Constants for 2D Materials Growth. *ACS Appl. Mater. Interfaces* **2017**, *9*, 11266-11271.

(48) Yadav, S. K.; Ramprasad, R. Strain-Assisted Bandgap Modulation in Zn Based II-VI Semiconductors. *Appl. Phys. Lett.* **2012**, *100*, 241903.

(49) Yadav, S. K.; Sadowski, T.; Ramprasad, R. Density Functional Theory Study of ZnX (X = O, S, Se, Te) under Uniaxial Strain. *Phys. Rev. B* **2010**, *81*, 144120.

(50) Lany, S.; Zunger, A. Assessment of Correction Methods for the Band-Gap Problem and for Finite-Size Effects in Supercell Defect Calculations: Case Studies for ZnO and GaAs. *Phys. Rev. B* **2008**, *78*, 235104.

(51) Daza, Y. A.; Maiti, D.; Kent, R. A.; Bhethanabotla, V. R.; Kuhn, J. N. Isothermal Reverse Water Gas Shift Chemical Looping on $La_{0.75}Sr_{0.25}Co_{(1-Y)}Fe_yO_3$ Perovskite Type Oxides. *Catal. Today* **2015**, *258, 2*, 691-698.

Email: jnkuhn@usf.edu (J.N.K.); bhethana@usf.edu (V.R.B.)

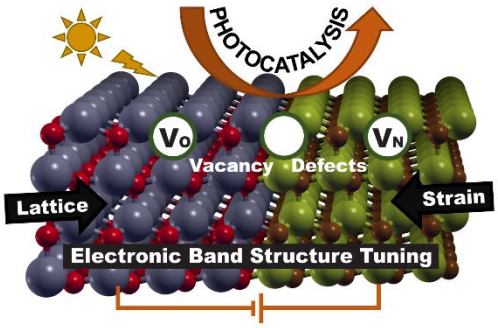

TOC Graphic

Email: jnkuhn@usf.edu (J.N.K.); bhethana@usf.edu (V.R.B.)